# Linear and non-linear vibrations of fluid-filled hollow microcantilevers interacting with small particles

Belardinelli, P.; Ghatkesar, M. K.; Staufer, U.; Alijani, F.

**DOI**
10.1016/j.ijnonlinmec.2017.04.016

**Publication date**
2017

**Document Version**
Accepted author manuscript

**Published in**
International Journal of Non-Linear Mechanics

Link to formal publication in International Journal of Non-Linear Mechanics (Elsevier): https://doi.org/10.1016/j.ijnonlinmec.2017.04.016

# Linear and non-linear vibrations of fluid-filled hollow microcantilevers interacting with small particles

P. Belardinelli[a], M.K. Ghatkesar[a], U. Staufer[a], F. Alijani[a,*]

[a]*Department of Precision and Microsystems Engineering, TU Delft, Netherlands*

**Abstract**

Linear and non-linear vibrations of a U-shaped hollow microcantilever beam filled with fluid and interacting with a small particle are investigated. The microfluidic device is assumed to be subjected to internal flowing fluid carrying a buoyant mass. The equations of motion are derived via extended Hamilton's principle and by using Euler-Bernoulli beam theory retaining geometric and inertial non-linearities. A reduced-order model is obtained applying Galerkin's method and solved by using a pseudo arc-length continuation and collocation scheme to perform bifurcation analysis and obtain frequency response curves. Direct time integration of the equations of motion has also been performed by using Adams-Moulton method to obtain time histories and analyze transient cantilever-particle interactions in depth. It is shown that exploiting near resonant non-linear behavior of the microcantilever could potentially yield enhanced sensor metrics. This is found to be due to the transitions that occur as a matter of particle movement near the saddle-node bifurcation points of the coupled system that lead to jumps between coexisting stable attractors.

*Keywords:* Non-linear vibrations, microbeam-particle interaction, transient response, microfluidics

## 1. Introduction

The characterization of cells and biological molecules in lab-on-a-chip devices is one of several goals reached by the Nano/Micro-Electro-Mechanical-Systems (NEMS/MEMS) technology in recent years. A wide and fast evolution, driven primarily by new advances in the fabrication processes, have led the sensors shrink in both size and mass, directing to new areas of investigations around previously unexplored experimental regimes [1, 2, 3].

Excellent dynamic characteristics of MEMS and NEMS resonators make them interesting tools for mass sensing and molecular interactions [4, 5]. Among different configurations, suspended cantilever resonators have shown superior qualities in terms of dynamic ranges and quality factors (QFs) comparing to doubly clamped beams [6]. The ability of these micro and nano tools for mass sensing is directly related to the fact that a decrease in the overall dimensions of the sensing device, corresponds to an increase in mass sensitivity, which is proportional to the resonant frequency of the cantilever and inversely proportional to its mass. Therefore, unprecedented sensitivity can be reached by inertial mass sensing [7] with Very High Frequency (VHF) nanobeams [8, 9]. Molecular mass measurements up to zeptogram [10] and attogram scale [11] have been achieved combining higher resonance frequencies and quality factors. The actual real limits of

*Corresponding author: Farbod Alijani, Department of Precision and Microsystems Engineering, 3ME, Mekelweg 2, (2628 CD) Delft, Netherlands. Tel.: +31 (0)15 27 86739. Email: f.alijani@tudelft.nl

these nanomechanical resonators are correlated to the imposed operating vacuum environment and fundamental physical noise processes with a resolution at the level of individual molecules [12, 13, 14].

For years, mass spectroscopy has been the primary method for weighing biomolecules [15] but this method often involves expensive equipments and massive laboratory settings. The biggest advantage of the traditional spectroscopy relies on the ability to distinguish samples that are chemically very similar. Nowadays, most of the efforts towards mass spectroscopy concerns mass labelling of biomolecules for early detection of diseases [16]. This has particularly been achieved by making use of nanomechanical resonators [17]. Yet, nanomechanical mass spectrometers, differently from traditional spectrometery that uses a potentially destructive ionization of the test sample, are more sensitive to large molecules. Moreover, their implementation on a chip is straightforward, enabling in vitro molecular recognitions such as protein markers of specific diseases [18, 19].

Bifurcation-based sensors are another class of MEMS/NEMS devices that exploit the sudden jumps of the frequency-amplitude response for sensing applications. The capability of such sensors in detecting both mass and position of a fixed particle located on the surface of a fully-clamped electrically-actuated beam has also been exploited [20]. The same technique has been also used in a piezoelectrically actuated microcantilever to detect gas molecules [21, 22].

Since inspection of biological samples requires aqueous environment, weighing biomolecules involves fluid-structure interaction. The measurement in fluid complicates the response of the sensor with a modification in the QF and in the resonant response [23]. The frequency shifts of a cantilever oscillating in different surrounding mediums have been observed [24]. In the work of Burg et al. [25], weighing biomolecules has been carried out by using a hollow cantilever known as "Suspended Microchannel Resonator (SMR)" . The experimental non-linear spring stiffening of SMRs with different lengths used for weighing nanoparticles in solution at the attogram scale is reported in the paper of Olcum et al. [26]. The dissipation phenomena in SMRs due to internal and external fluid effects has also been addressed in the literature [27, 28]. The energy dissipation caused by internal flow is found to be non-monotonic with respect to the viscosity of the filling medium [29]. Moreover, it is found that the fluid velocity in SMRs is affected both by the position and deformation of the embedded channel [30], as well as the oscillation mode [31].

As it can be perceived, the published literature on using cantilevers for mass sensing applications are quite abundant. However, non-linear dynamics of these systems interacting with flowing particles has not yet been addressed. Therefore, this paper undertakes modelling and simulations of a hollow microcantilever beam in the linear and non-linear domain filled with a fluid and subjected to a flowing particle. The hollow cantilever under investigation is shown in Figure 1. The hollow cantilever is made of silicon dioxide and it has two on-chip reservoirs. The U-shaped cantilever is connected between these reservoirs. The fabrication details of the device are given elsewhere [32].

The microfluidic device has two legs with an internal channel. Therefore, in the present work, the particular geometry is described by means of discontinuous functions due to the variation of the cross section. The equations of motion are obtained by using non-linear Euler-Bernoulli beam theory retaining geometric and inertia non-linearities. The resulting system of equations is then reduced to a set of ordinary-differential equations by applying Galerkin technique. A psuedo arc-length continuation algorithm and Adams-Moulton direct time integration have been used to investigate the particle-beam transient response. The rich dynamics of the hollow cantilever are discussed, including a parametric study with the external harmonic excitation frequency used as the parameter to amplify the effects of the particle interaction. The focus is on obtaining the frequency-amplitude responses to be exploited for mass sensing applications.

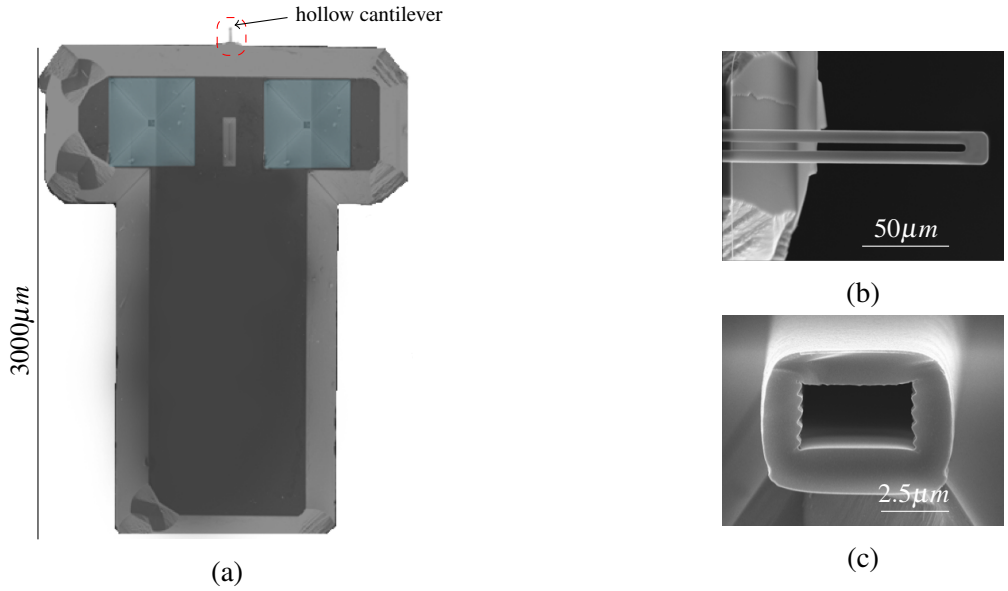


Figure 1: Hollow cantilever chip. a) Back side of the chip where the cantilever is located; b) U-shaped cantilever; c) cross-section of the hollow cantilever.

## 2. Problem definition

The device illustrated in Figure 1 is modeled as a hollow cantilever beam with length $L$ and rectangular cross section in an orthogonal coordinate system $(O;x,y,z)$ with unit vectors $\mathbf{i},\mathbf{j},\mathbf{k}$ as shown in Figure $2(a,b)$. The beam is assumed to be made of isotropic material and is composed of two legs with an embedded microchannel that is subjected to an inviscid axial flow while carrying a particle of mass $M$. Figure $2(c)$ shows part of the deformed configuration with length $s$ in base inertial $(x,z)$ and body coordinate $(\xi,\theta)$ systems in which $\psi=\psi(s,t)$ is the rotation angle between $\xi$ and $x$. The curvilinear coordinate $X$, measured along the center arc length of the beam, indicates the position of the mass.

As a consequence of having the embedded microchannel, the geometric properties of the hollow cantilever cannot be considered constant. Therefore, the variation in the area of the beam cross section is written as

$$A=A(s)=A_1H_0+A_0H_{l_0}-A_2(H_{l_1}-H_{l_2})+A_3H_{l_2}, \tag{1}$$

in which $H_{l_i}=H(s-l_i)$ for $i=0,1,2$ (shown $l_i$ in Figure $2(a)$) and $H_0=H(s)$, $H$ being the Heaviside function defined as:

$$H(s)=\begin{cases}1 & \text{if } s\geq 0,\\ 0 & \text{if } s<0.\end{cases} \tag{2}$$

Figure $2(b)$ sketches the non-uniform cross sections of the beam having total thickness $t_0$, total width $B$, and partial areas $A_0=(B-2w_0)t_0$, $A_1=2(w_0t_0-w_1t_1)$, $A_2=(B-w_0-w_1)t_1$ and $A_3=2w_1t_1$. Thus, the mass per unit length of the beam with constant density $\rho$ is given by

$$m_b=m_b(s)=\rho A(s), \tag{3}$$

The area of the embedded microchannel is similarly defined and permits to describe the internal fluid cross section as:

$$A_f=A_f(s)=A_{f_{leg_1}}+A_{f_{leg_2}}+A_{f_{end}}. \tag{4}$$

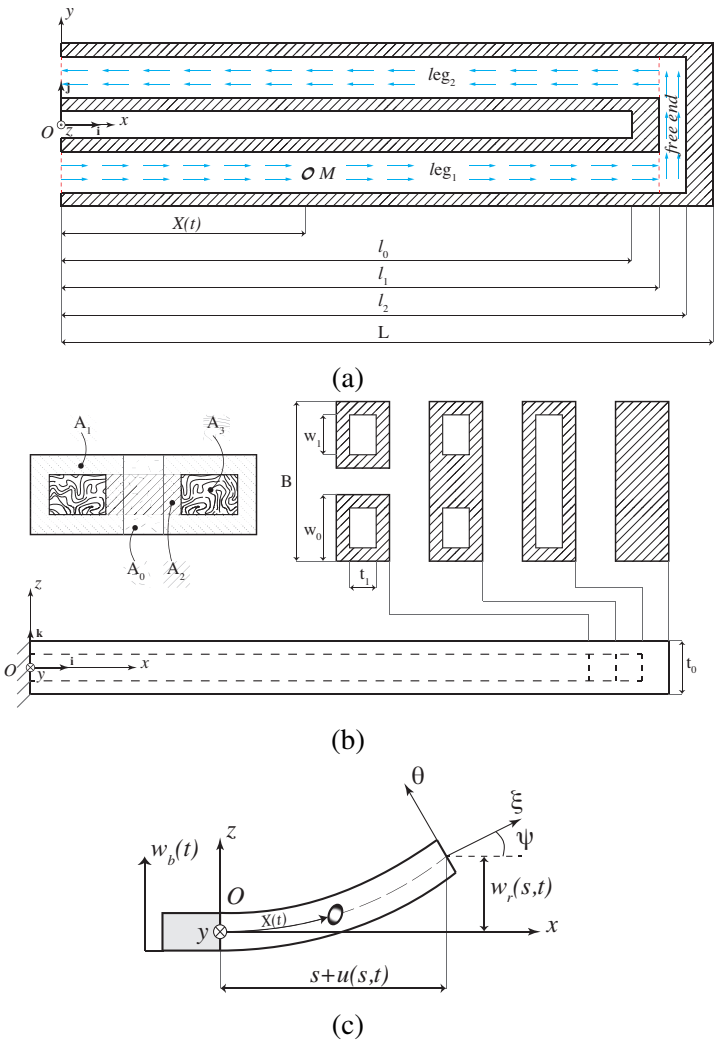


Figure 2: Hollow cantilever beam. a) A schematic view of the sectioned hollow cantilever carrying a particle. The dashed lines represent the internal channel path; b) the cross section with symmetry in $x$ and $y$; c) sketch of the deformed configuration with inertial and body coordinate systems.

$A_{f\,leg_1} = A_{f\,leg_2} = \dfrac{A_3}{2}(H_0 - H_{l_1})$ and $A_{f\,end} = (A_2 + A_3)(H_{l_1} - H_{l_2})$, are the areas of the first, second leg, and free-end, respectively. $m_f = m_f(s) = \rho_f A_f(s)$ is the mass of internal fluid per unit length, and $\rho_f$ is the density of the fluid filling the microchannel. The symbol $m = m(s) = m_b + m_f$ indicates the mass of the beam per unit length accounting for the filling fluid. Due to symmetry, the total mass filling each leg of the beam is $m_{f\,leg_1} = m_{f\,leg_2} = \rho_f \dfrac{A_3}{2} l_1$. Moreover, the total mass of the fluid at the free-end is $m_{f\,end} = \rho_f (A_3 + A_2)(l_2 - l_1)$. The moment inertia of the beam can be defined accordingly as:

$$I = I(s) = I_1 H_0 + I_0 H_{l_0} - I_2 (H_{l_1} - H_{l_2}) + I_3 H_{l_2}, \tag{5}$$

where $I_0 = \frac{(B-2w_0){t_0}^3}{12}$, $I_1 = \frac{1}{6}\left(w_0{t_0}^3 - w_1{t_1}^3\right)$, $I_2 = \frac{(B-w_0-w_1){t_1}^3}{12}$, $I_3 = \frac{w_1{t_1}^3}{6}$.

## 3. Equations of motions

The longitudinal and transverse displacements of the beam with respect to the clamped base are $u(s,t)$ and $w_r(s,t)$as shown in Figure $2(c)$. The total transverse displacement of the beam

accounting for the base motion $w_b(t)$ [33], is

$$w(s,t) = w_b(t) + w_r(s,t), \tag{6}$$

where $w_b = Z\cos(\omega t)$, in which $Z$ and $\omega$ are amplitude and frequency of the base motion, respectively.

By definition, the velocity of the beam element shown in Figure 2$(c)$ is $\mathbf{U}_b = \dot{x}\mathbf{i} + (\dot{z} + \dot{w_b})\mathbf{k}$ in which $\dot{x} = \dot{u}$ and $\dot{z} = \dot{w_r}$. As usual, overdot means differentiation with respect to time. Moreover, the velocity of the fluid is $\mathbf{U}_f = \mathbf{U}_b \pm V\tau$ where $\pm V\tau$ is the relative velocity of the fluid with respect to the beam. The positive sign indicates the fluid flowing in $leg_1$ and negative in $leg_2$. Since we assume the inextensibility of the beam over deformation, that is

$$\left(1 + u'\right)^2 + {w_r'}^2 = 1, \tag{7}$$

the unit vector in $\xi$ direction has the form

$$\tau = x'\mathbf{i} + z'\mathbf{k} = \left(1 + u'\right)\mathbf{i} + w_r'\mathbf{k}, \tag{8}$$

in which prime denotes derivative with respect to the position $s$. It can also be observed that Eq. (7) allows to reduce the dependent variables from two to one since $u' \approx -\frac{1}{2}w'^2$. For a cantilever without external load applied at the free edge the explicit relationship of $u$ as a function of $w$ is:

$$u = -\frac{1}{2}\int_0^s {w_r'}^2 ds. \tag{9}$$

Therefore, by making use of Eq. (7) the expression of the fluid element is :

$$\mathbf{U}_f = \left(\dot{u} \pm V\left(1 + u'\right)\right)\mathbf{i} + \left(\dot{w} \pm V w_r'\right)\mathbf{k}. \tag{10}$$

Here, it should be noted that the fluid velocity at the free-end contributes to the motion in $y$ direction which is not accounted in the beam theory utilized in this paper. Moreover, this effect comes to play for a relatively short time due to the ratio between the width and the length of the channel, and therefore can be neglected in real sensing applications [11].

An energy approach has been used to obtain the governing equations of motion. Since each leg that composes the beam is an open system, Hamilton's principle for systems with an open control volume should be applied. Here, we assume that the fluid entrance and exit conditions over $leg_1$ and $leg_2$ are prescribed and constant. Hamilton's principle yields [34]:

$$\delta\int_{t_1}^{t_2}\mathscr{L}dt + \int_{t_1}^{t_2}\delta\mathscr{W}_{nc}dt = \int_{t_1}^{t_2} m_{f_{leg_1}} V\left(\dot{\mathbf{r}}_{l_1} + V\tau\right)\cdot\delta\mathbf{r}_{l_1}dt - \int_{t_1}^{t_2} m_{f_{leg_2}} V\left(\dot{\mathbf{r}}_{l_1} - V\tau\right)\cdot\delta\mathbf{r}_{l_1}dt, \tag{11}$$

where $\mathscr{L}$ is the Lagrangian of the system and $\delta\mathscr{W}_{nc}$ is the work associated with the nonconservative forces acting on the system. Moreover, $\delta\mathbf{r}_{l_1}$ is the variation of the position of the fluid at the open (flow) area, $\delta\mathbf{r}_{l_1} = \delta u_{l_1}\mathbf{i} + \delta w_{l_1}\mathbf{k}$. Therefore, by using Eq.(8), the right hand side of Eq. (11) can be rewritten as

$$2\int_{t_1}^{t_2} m_{f_{leg_1}}\left(V^2\left(1 - \frac{1}{2}w_{r_{l_1}}^2\right)\delta u_{l_1} + w_{l_1}'\delta w_{rl_1}\right)dt. \tag{12}$$

By making use of Eqs. (9) and (4) and neglecting higher-order terms (i.e. $\frac{1}{2}w_{r_{l_1}}^2\delta u_{l_1}$) [34], Eq. (12) reduces to

$$2\int_{t_1}^{t_2} m_{f_{leg_1}} V^2\left(-\int_0^{l_1} {w_r}'\delta {w_r}' ds + w_{l_1}'\delta w_{rl_1}\right)dt = \int_{t_1}^{t_2} V^2\int_0^L m_f\left(H_0 - H_{l_1}\right){w_r}''\delta w_r ds dt \tag{13}$$

after integration by parts.

The dissipation in the system is herein accounted in Eq. (11) by

$$\delta \mathscr{W}_{nc} = -\int_0^L c\dot{w}_r \delta w_r ds, \tag{14}$$

that represents a linear damping force with $c$ being the viscous damping coefficient.

The expression for the Lagrangian is defined as follows

$$\mathscr{L} = T - \Pi + \frac{1}{2}\int_0^L \lambda \left[1 - w_r'^2 - \left(1+u'\right)^2\right] ds, \tag{15}$$

where $\lambda(x,t)$ is the Lagrange multiplier that has been added to the Lagrangian in order to account for the inextensibility condition given by Eq. (7), $T$ and $\Pi$ are the kinetic and the elastic energy, respectively.

The elastic energy of the beam assuming Euler-Bernoulli beam theory and neglecting shear deformation and rotary inertia can be obtained as

$$\Pi = \frac{1}{2}\int_0^L EI\left(\psi'\right)^2 ds, \tag{16}$$

in which $E$ is the Young's modulus, and $I$ is the nonuniform inertia obtained from Eq.(5). Furthermore, $\psi'$ is the curvature that can be written as a function of $u$ and $w$, [35]:

$$\psi' = w_r''\left(1+u'\right) - w_r' u''. \tag{17}$$

The kinetic energy of the system $T$ includes that of the beam $T_b$, the fluid $T_f$ and the moving mass $T_m$. For the beam, the kinetic energy can be obtained neglecting the rotatory inertia as follows

$$T_b = \frac{1}{2}\int_0^L m_b\left(\dot{u}^2 + \dot{w}^2\right) ds. \tag{18}$$

The kinetic energy of the fluid using Eqs.(7) and (10) can be obtained as:

$$T_f = \frac{1}{2}\left(m_{f\,leg1} + m_{f\,leg2}\right)\int_0^{l_1}\left[\dot{u}^2 + \dot{w}^2 + V^2\right] ds + \frac{1}{2} m_{f\,end}\int_{l_1}^{l_2}\left[\dot{u}^2 + \dot{w}^2\right] ds. \tag{19}$$

The kinetic energy of the moving mass is defined in a similar fashion as:

$$T_m = \frac{1}{2} M\left[\left(\dot{u} + V\left(1+u'\right)\right)^2 + \left(\dot{w} + V w_r'\right)^2\right]_{s=X(t)}. \tag{20}$$

Here it is assumed that the mass $M$ is transported with constant velocity by the internal flowing fluid along the channel, thus its instantaneous position is $X = Vt$.

Taking the variation of the kinetic energy yields:

$$\begin{aligned} &\delta\int_{t_1}^{t_2} T dt = \int_{t_1}^{t_2}\int_0^L \left(m_b + m_f\right)\left(\ddot{u}\delta u + \ddot{w}\delta w_r\right) ds + \\ &M\left[\left(\ddot{u} + \dot{V}\left(1+u'\right) + 2V\dot{u}' + V^2 u''\right)\delta u + \left(\ddot{w} + \dot{V} w_r' + 2V\dot{w}_r' + V^2 w_r''\right)\delta w_r\right]_{s=X(t)} dt, \end{aligned} \tag{21}$$

in which the integral with respect to the spatial coordinate $s$ represents the inertial effect of the beam and fluid masses. It can be noted that although the system presents a flowing fluid, the flow in the opposite directions eliminates all the possible inertial effects due to the relative motion of the

fluid with respect to the beam. The second term within the integral in time in Eq.(21) is the effect of the flowing particle acting locally inside the beam. Here, for both the variations in $\delta u$ and $\delta w_r$, four terms introduce the coupling between the particle and the beam. The first term is the inertial effect of the particle proportional to its acceleration, the second (related to $\dot{V}$) comes from the particle acceleration. Finally, the third and fourth terms represent the Coriolis and the centripetal accelerations, respectively [36]. Here it shall be noted that for the particle: (i) $u = u\left(X\left(t\right),t\right)$ and $w = \left(X\left(t\right),t\right)$; (ii) $\dot{V} = 0$. Therefore, the equations for the variations $\delta u$ and $\delta w_r$ become

$$\int_0^L \left[ m\ddot{u} - \left( E w_r' \left( I w_r'' \right)' + \lambda \left( 1 + u' \right) \right)' \right] ds + M \left[ \ddot{u} + 2V\dot{u}' + V^2 u'' \right]_{s=X(t)} = 0 \tag{22}$$

$$\int_0^L \left[ m\ddot{w} + c\dot{w}_r + E\left( I w_r'' \right)'' + V^2 m_f \left( H_0 - H_{l_1} \right) w_r'' + E\left( I w_r' w_r''^2 \right)' - \left( \lambda w_r' \right)' \right] ds + M \left[ \ddot{w} + 2V\dot{w}_r' + V^2 w_r'' \right]_{s=X(t)} = 0 \tag{23}$$

From equations (22) and (9), $\lambda$ could be explicitly obtained as

$$\lambda = \left( 1 - \frac{1}{2} w_r'^2 \right)^{-1} \left\{ -E w_r' \left( I w_r'' \right)' - \frac{1}{2} \int_L^s m \left( \int_0^s \ddot{w_r}^2 ds \right) ds - \int_L^s \frac{M}{L} \left[ \frac{1}{2} \int_0^s \ddot{w_r}^2 ds + V\dot{w_r}^2 + V^2 w_r' w_r'' \right] \delta_\Delta \left( s - X \right) ds \right\}. \tag{24}$$

where $\delta_\Delta$ is the Dirac-Delta function. Expanding the multiplier up to cubic order yields [37]:

$$\lambda = -E w_r' \left( I w_r'' \right)' - \frac{1}{2} \int_L^s m \left( \int_0^s \ddot{w_r}^2 ds \right) ds - \int_L^s \frac{M}{L} \left[ \frac{1}{2} \int_0^s \ddot{w_r}^2 dx + V\dot{w_r}^2 + V^2 w_r' w_r'' \right] \delta_\Delta \left( s - X \right) ds. \tag{25}$$

The equation of motion is finally found by substituting the expression for Lagrange multiplier into (23) as follows:

$$\begin{aligned} & m\ddot{w}_r + E\left( I w_r'' \right)'' + c\dot{w}_r + V^2 m_f \left( H_0 - H_{l_1} \right) w_r'' + E\left( I w_r' w_r''^2 \right)' + E\left( w_r'^2 \left( I w_r'' \right)' \right)' + \left[ w_r' \int_L^s m \left( \int_0^s w_r' \ddot{w}_r' + \dot{w_r}^2 ds \right) ds \right]' \\ & + \left( w_r' \int_L^s \frac{M}{L} \left[ \frac{1}{2} \int_0^s \ddot{w_r}^2 ds + V\dot{w_r}^2 + V^2 w_r' w_r'' \right] \delta_\Delta \left( s - X \right) ds \right)' + \frac{M}{L} \left[ \ddot{w} + 2V\dot{w}_r' + V^2 w_r'' \right] \delta_\Delta \left( s - X \right) = -m\ddot{w}_b. \end{aligned} \tag{26}$$

### *3.1. Discretized model*

For convenience we express the governing equations of motion in dimensionless form

$$\begin{aligned} & \hat{m}\ddot{\hat{w}}_r + \hat{c}\dot{\hat{w}}_r + \left( \hat{I}\hat{w}_r'' \right)'' + \hat{V}^2 \hat{m}_f \left( \hat{H}_0 - \hat{H}_{\hat{l}_1} \right) \hat{w}_r'' + \left( \hat{I}\hat{w}_r' \hat{w}_r''^2 \right)' + \left( \hat{w}_r'^2 \left( \hat{I}\hat{w}_r'' \right)' \right)' + \\ & \left[ \hat{w}_r' \int_1^{\hat{s}} \hat{m} \left( \int_0^{\hat{s}} \hat{w}_r' \ddot{\hat{w}}_r' + \dot{\hat{w}}_r'^2 d\hat{s} \right) d\hat{s} \right]' + \left( w_r' \int_1^{\hat{s}} \hat{M} \left[ \frac{1}{2} \int_0^{\hat{s}} \ddot{w_r}^2 d\hat{s} + \hat{V}\dot{w_r}^2 + \hat{V}^2 w_r' w_r'' \right] \hat{\delta}_\Delta \left( \hat{s} - \hat{X} \right) d\hat{s} \right)' + \\ & \hat{M} \left[ \ddot{\hat{w}}_r + 2\hat{V}\dot{\hat{w}}_r' + \hat{V}^2 \hat{w}_r'' \right] \hat{\delta}_\Delta \left( \hat{s} - \hat{X} \right) = \left( \hat{m} + \hat{M}\hat{\delta}_\Delta \left( \hat{s} - \hat{X} \right) \right) \hat{G} \cos\left( \hat{\omega}\hat{t} \right). \end{aligned} \tag{27}$$

The complete set of expressions for the dimensionless variables and parameters are reported in Appendix A.

In order to study the dynamics of the cantilever, a reduced-order model is built, converting the partial differential equation (27) to a set of non-linear ordinary differential equations. Hence, first the transverse displacement $\hat{w}_r$ is expanded in terms of admissible functions satisfying the boundary conditions:

$$\hat{w}_r \left( \hat{s}, \hat{t} \right) = \sum_n \phi_n \left( \hat{s} \right) q_n \left( \hat{t} \right) \tag{28}$$

where $q_n(\tau)$ are the generalized temporal coordinates, and $\phi_n(\hat{s})$ are the linear modes of the cantilever beam normalized such that $\int_0^1 \phi_n^2(\hat{s})\,ds = 1$:

$$\phi_n(\hat{s}) = \cosh(\Lambda_n \hat{s}) - \cos(\Lambda_n \hat{s}) + \frac{\cosh(\Lambda_n)+\cos(\Lambda_n)}{\sin(\Lambda_n)+\sinh(\Lambda_n)}\left[\sin(\Lambda_n \hat{s}) - \sinh(\Lambda_n \hat{s})\right], \tag{29}$$

the eigenfrequencies $\omega_n = \Lambda_n^2$ are obtained from the dispersion equation

$$1 + \cos(\Lambda_n)\cosh(\Lambda_n) = 0. \tag{30}$$

Next, by applying Galerkin's method, the discretized equations can be obtained as follows

$$I_{1\,jn}\ddot{q}_n + \left(I_{2\,jn} + I_{6\,jn}\right) q_n + \left(I_{3\,jnmk} + I_{4\,jnmk}\right) q_n q_m q_k + I_{5\,jnmk}\left(q_n q_m \ddot{q}_k + q_n \dot{q}_m \dot{q}_k\right) + \hat{c} I_{7\,jn}\dot{q}_n + F_{part} = \hat{G} I_{8\,j}\cos(\hat{\omega}\hat{t}) \tag{31}$$

in which the particle interaction function $F_{part}$, taking into account the full motion of the particle along the entire channel is:

$$F_{part} = \alpha^2 \hat{M}\hat{V}^2 \phi_n''(\hat{X})\,\phi_j(\hat{X})\,q_n + 2\alpha \hat{M}\hat{V}\phi_n'(\hat{X})\,\phi_j(\hat{X})\,\dot{q}_n + \hat{M}\phi_n(\hat{X})\,\phi_j(\hat{X})\,\ddot{q}_n + \alpha^2 I_{9\,jnmk} q_n q_m q_k + \alpha I_{10\,jnmk} q_n \dot{q}_m \dot{q}_k + I_{11\,jnmk}\left(q_n \dot{q}_m \dot{q}_k + q_n q_m \ddot{q}_k\right) \tag{32}$$

$$\alpha = \begin{cases} +1 & \text{if} \quad 0 \le \hat{X} < \hat{l}_1 \\ 0 & \text{if} \quad \hat{X} = \hat{l}_1 \\ -1 & \text{if} \quad 0 \le \hat{X} < \hat{l}_1, \quad \hat{t} \ge \left(\hat{l}_1 + \hat{B}\right)/\hat{V}. \end{cases} \tag{33}$$

At the free-end of the beam, the mass travels along the $y$ direction, and in the presented one-dimensional model, it is stationary at a specific location. The integrals $I_i$ for $i = 1,..11$ in Eqs.(31)-(32) are given in Appendix B. The terms $I_{1,2}$ account for the global mass and the stiffness of the beam whereas $I_6$ is related to the flowing fluid. The integrals $I_{3,4}$ govern the geometric non-linearities while the inertia non-linearities are driven by $I_5$. The linear damping is correlated with $I_7$, the base excitation with $I_8$. Finally, $I_i$ for $i = 9,..11$ derive from the particle influence on the longitudinal equation of motion. The particle interaction is a time dependent effect acting locally and modelled in Eq. (27) by a function that shall be evaluated at the specific position of the particle.

## 4. Results and discussions

The procedure outlined in previous sections has been used to numerically study linear and non-linear vibrations of the silicon dioxide hollow cantilever shown in Figure 1. Numerical values that are used in the analyses are listed in Table 1. Note that Eq.(31) represents an infinite number of ordinary differential equations with geometric and inertia non-linearities that shall be written in state space form for numerical implementation. In order to characterize the non-linear response of the cantilever and the fluid-structure interaction problem in the absence of particle and for the particle located at specific positions, a pseudo-arc length continuation and collocation technique have been used [38]. In particular, a bifurcation analysis is performed in three steps: (i) The bifurcation analysis begins at zero force level where the initial solution is the trivial undisturbed configuration of the hollow cantilever by considering fluid velocity as the first bifurcation parameter at fixed excitation frequency far from the fundamental frequency; (ii) Once the desired flow velocity is

reached, the bifurcation analysis continues by considering the amplitude of the harmonic excitation, $\hat{Z}$ , as the continuation parameter and is increased till it reaches the desired force level; (iii) Once the desired force amplitude is reached, the bifurcation analysis continues by considering the excitation frequency as the continuation parameter to obtain the frequency-amplitude response of the cantilever (at fixed excitation amplitude and for an assigned value of fluid velocity). In the presence of moving particle, as a consequence of the transient vibrations induced by the particle, direct time integration of the equations of motion has also been performed by using a multistep Adams-Moulton method.

In what follows, unless otherwise specified, the cantilever is assumed to be filled with water with a global $QF = 500$ [39, 40]. Moreover, a mass of $20pg$ is considered transported, i.e. without relative motion with respect to the fluid and with constant velocity.

| Parameter | Symbol | Unit | Value |
|---|---|---|---|
| Cantilever length | $L$ | $\mu m$ | 155 |
| Cantilever width | $B$ | $\mu m$ | 16.08 |
| Cantilever height | $t_0$ | $\mu m$ | 4.9 |
| Beam density | $\rho$ | $kg/m^3$ | 2200 |
| Young's modulus | $E$ | $GPa$ | 87 |
| Leg separation length | $l_0$ | $\mu m$ | 143.8 |
| Leg width | $w_0$ | $\mu m$ | 6.4 |
| Fluid channel length (lower) | $l_1$ | $\mu m$ | 146.8 |
| Fluid channel max length | $l_2$ | $\mu m$ | 153.5 |
| Fluid channel width | $w_1$ | $\mu m$ | 3.7 |
| Fluid channel height | $t_1$ | $\mu m$ | 2.2 |

Table 1: Geometric and physical characteristics of the hollow cantilever (see Figure 2).

The accuracy and convergence of the model can be examined by considering different number of generalized coordinates in Eq.(31). Figure 3 shows the convergence rate of the response for models with different number of generalized coordinates. The frequency-response curves are obtained in the frequency neighbourhood of the fundamental mode. In this case the hollow cantilever is filled with water and is subjected to a harmonic force at the base with different dimensionless amplitudes $\hat{Z} = \{0.00003, 0.0001, 0.0003\}$, showing a transition from linear to hardening behavior. The convergence appeared to be quite fast and good balance between precision and computational time is obtained if only three transverse modes are included in the model.

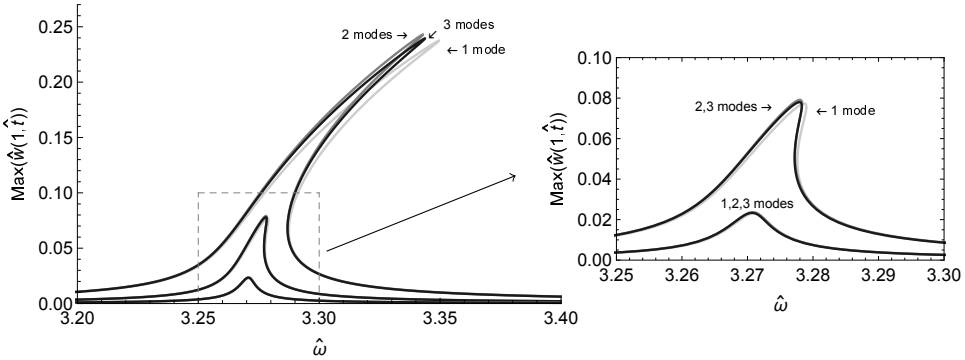


Figure 3: Effect of number of modes retained in the expansion (31) for the hollow cantilever beam filled with water when $\hat{Z} = \{0.00003, 0.0001, 0.0003\}$ and $QF = 500$.

In order to validate the accuracy of the new model, we present a comparison by reducing the hollow cantilever to a rectangular homogeneous silicon microbeam ($l_0 = w_1 = t_1 = 0$, $l_1 = l_2$), with the response obtained by Mahmoodi et al. [41]. For this comparison $L = 46\mu m$, $B = 50\mu m$, $t_0 = 2\mu m$. In Figure 4 the results presented in Figure 10(b) of Ref. [41] are repeated and compared to the numerical simulations with the present model. Here, $\sigma$ is the detuning parameter $\sigma = \left(\hat{\omega}/\sqrt{I_{1_{11}}/I_{2_{11}}} - 1\right)$, $\hat{\omega}$ is the nondimensional excitation frequency and $I_{1,2}$ are defined in Appendix B. Good agreement can be observed with a similar qualitative hardening non-linearity. The small deviation in the results can be attributed to the approximations that are made to convert the hollow cantilever to a uniform rectangular cantilever.

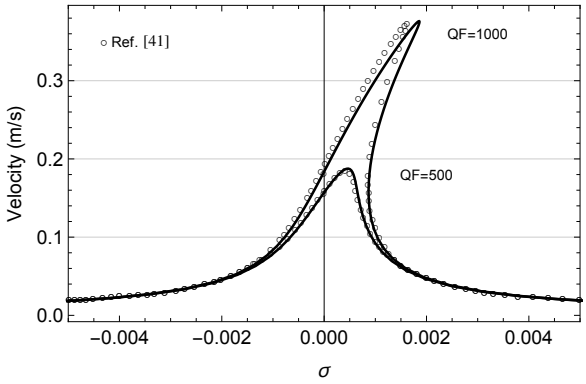


Figure 4: Comparison of the result presented in Figure 10(b) of Ref. [41] (○) with that replicated by means of the current model (solid line). For the simulations, three modes are retained in the discretization.

In order to check the validity of the present model when filled with fluid, the first three natural frequencies of the empty and fluid filled cantilever have been compared to those obtained from finite element software Comsol. A good agreement is observed for both the empty and the filled cases also by considering different fluids with a maximum deviation of around 2.1%.

| | Empty | | | Ethanol | | | $H_2O$ | | | Deuterium Oxide ($D_2O$) | | |
|---|---|---|---|---|---|---|---|---|---|---|---|---|
| Mode | $1^{st}$ | $2^{st}$ | $3^{rd}$ | $1^{st}$ | $2^{st}$ | $3^{rd}$ | $1^{st}$ | $2^{st}$ | $3^{rd}$ | $1^{st}$ | $2^{st}$ | $3^{rd}$ |
| Present model | 235.3 | 1469.7 | 4093.5 | 221.3 | 1380.8 | 3861.3 | 218.0 | 1359.6 | 3802.3 | 216.4 | 1349.9 | 3786.1 |
| Finite Element Package (Comsol) | 233.8 | 1453.2 | 4022.4 | 219.5 | 1368.7 | 3788.5 | 216.3 | 1348.6 | 3732.9 | 214.8 | 1339.3 | 3707.8 |

Table 2: Comparison of the first three natural frequencies of empty and fluid filled hollow cantilever (values unit kHz).

Figure 5 shows the maximum deflection of the cantilever in time domain when it is excited harmonically by dimensionless amplitude and frequency $\hat{Z} = 0.000015$, $\hat{\omega} = 3.268$ and is subjected to a moving particle with a velocity of $0.004m/s$. The plot reports four vertical dashed lines corresponding to four distinct instants in time. The first line corresponds to the instant in which the particle enters the channel; the second and the third are the start and the end of the motion in the $y$ direction, respectively (in our one-dimensional model the particle is fixed at $\hat{X} = \hat{l}_1$ (see Eq.(32))). Finally, the last line represents the point at which particle leaves the channel. It can be observed that the presence of moving particle inside the channel changes the steady state response of the cantilever.

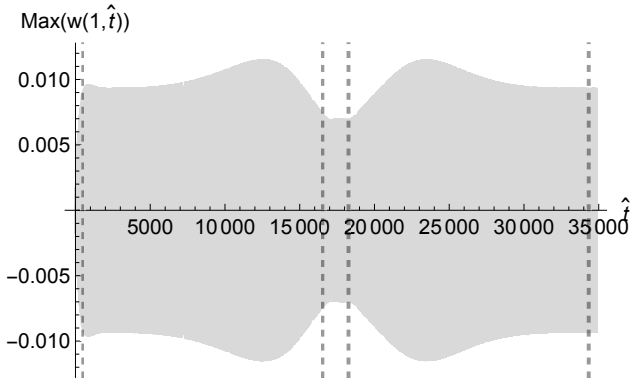


Figure 5: Time response of the beam during linear motion when $\hat{Z} = 0.000015$ and $\hat{\omega} = 3.268$. The moving particle has $M = 20pg$ and a velocity of $0.004m/s$. The time history is evaluated for the complete travel of the particle inside the two legs of the beam.

The response shown in Figure 5 is discussed in more details in Figure 6$(a,b)$ when the particle is passing through the first leg of the cantilever only. It can be seen that since the chosen excitation frequency is close to the fundamental frequency of the beam, the motion is primarily driven by the first mode with an increase in the amplitude of the oscillation. This could also be interpreted from the discrete time instants $A$,$B$,$C$ and $D$ in Figure 6$(a)$. This monotonic behaviour is interrupted at $\hat{t} = 12600$ where the amplitude of the motion starts to decrease (points $E$ and $F$ of Figure 6).

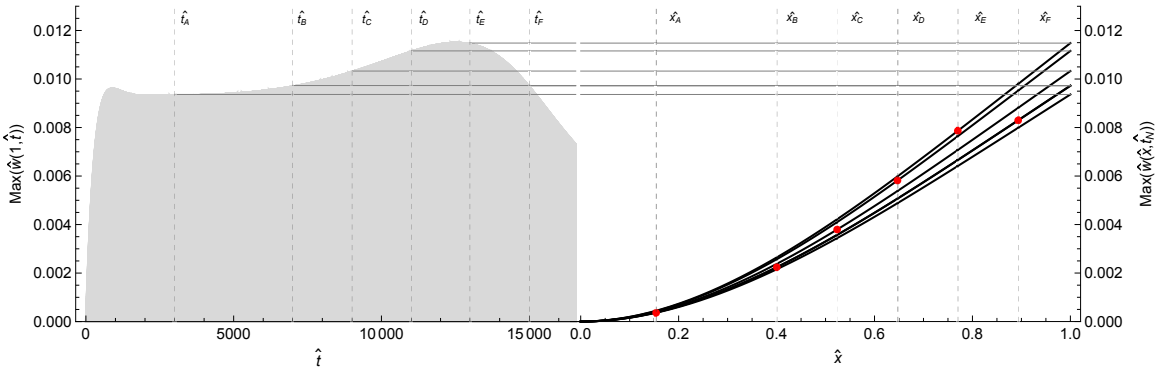


(a)

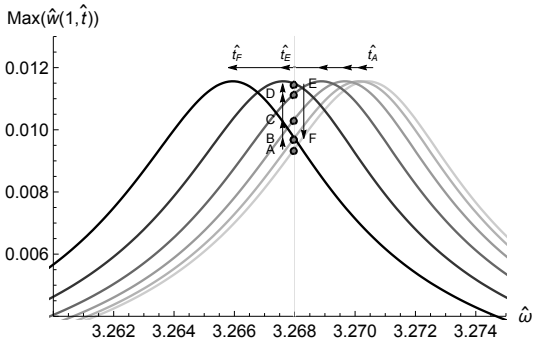


(b)

Figure 6: Particle influence on the beam response with the same simulation parameters of Figure 5. Points *A*-*F* depict different time instants at which the particle lies at specific position along the first leg of the channel (shown as red dots). (a) Amplitude of the beam as a function of time for the particle travelling along one leg of the beam. (b). Frequency response curve translation due to the particle movement. The upper horizontal arrows indicate the translation of the resonant peak.

The frequency response curves associated with discrete time instants *A*-*F* are shown in Figure 6$(b)$. It can be observed that the movement of the particle changes the frequency response curve, shifting the curve to the left side of the excitation point $\hat{\omega} = 3.268$. As a consequence, as long as the peak amplitude of the frequency response curve is above the amplitude of the excitation frequency the particle runs on the left branch. Therefore, the amplitude of the motion continues to grow monotonically as the particle approaches the free-end (moving from point *A* - *D* ). Once the particle passes the peak amplitude then the amplitude drops from *E*-*F* as a mater of particle moving along the right branch of the frequency response curve.

The time response envelopes of the hollow cantilever subjected to the same moving particle are shown in Figure 7 for different excitation frequencies before and after the resonance frequency. The frequency response curve shown in the figure is for the case without added particle. Four different excitation frequencies are chosen and for each the time response envelope is shown in an inset figure. Starting far from the resonant frequency the amplitude is low and the translation of the curve caused by the particle is not enough to observe the peak; as a matter of fact particle is moving only along the left branch of the frequency response curve. By approaching the resonant frequency (e.g. $\hat{\omega} = 3.266$), the initial amplitude increases following a decrease as a consequence of passing the peak amplitude. Conversely, a relative offset beyond the resonant frequency (e.g. $\hat{\omega} = 3.272$) decreases the amplitude of the response continuously.

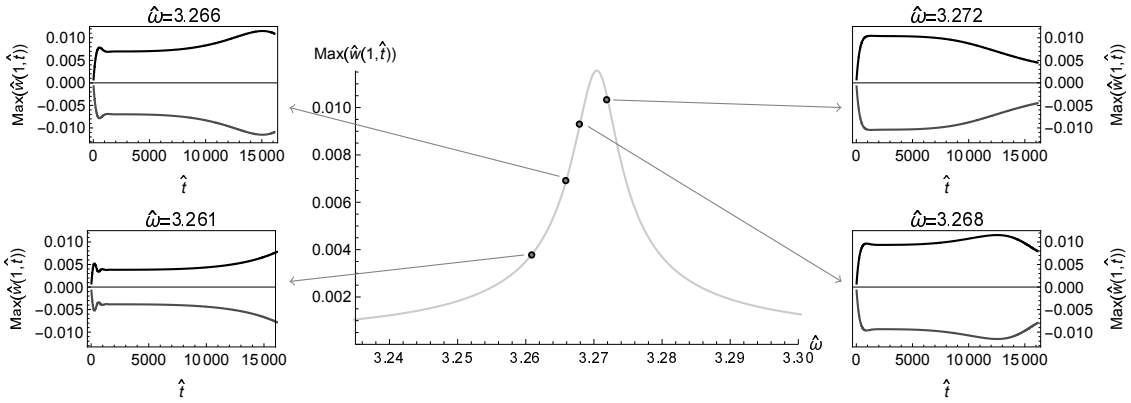


Figure 7: Time response envelops of the hollow cantilever excited at different excitation frequencies and subjected to moving particle. The response is shown for the particle passing only the first leg of the hollow cantilever.

As it can be perceived, the final response highly depends on the excitation frequency. In fact, the combined effect of amplitude growth and reduction is only possible if the cantilever is excited with an offset below the resonant frequency.

Figure 8 shows the reduction in the frequency as a function of particle travelling time for different excitation frequencies till $\hat{X} = \hat{l}_1$. This reduction is associated with the variation in the response amplitude described previously that highly depends on the particle position and the excitation frequency. Thus, if the final purpose is to exploit the frequency drop for mass-sensing, the fundamental step is to locate the correct range of beam parameters such that maximum frequency resolution is achieved (e.g. in this case when $\hat{\omega} = 3.265$), potentially eliminating the need for sophisticated frequency tracking hardware [22, 25].

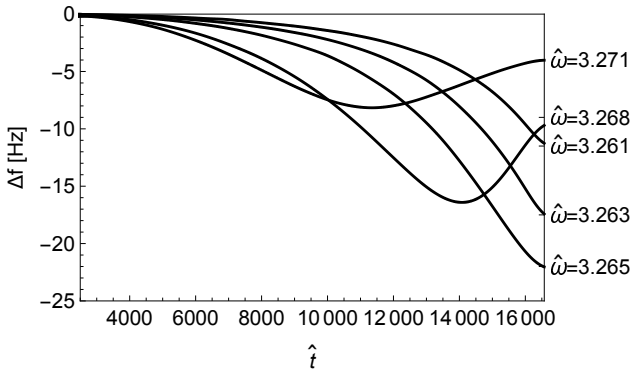


Figure 8: Frequency drop as a function of the travelling time ($V = 0.004m/s$) in the hollow cantilever carrying a mass of $20pg$ for one leg travel of the particle. The frequency reduction is compared to the fundamental frequency of the beam without particle interaction.

Figure 9 compares the non-linear frequency amplitude response of the empty cantilever with cantilevers filled with $D_2O$, $H_2O$ and Ethanol. As it can be observed the presence of liquid inside the channel decreases the fundamental frequency similar to the linear case (see Table 2), while it has a trivial effect on the trend of non-linearity. In fact the strength of non-linearity may change at sufficiently large flow velocities which are not the case in real sensing applications.

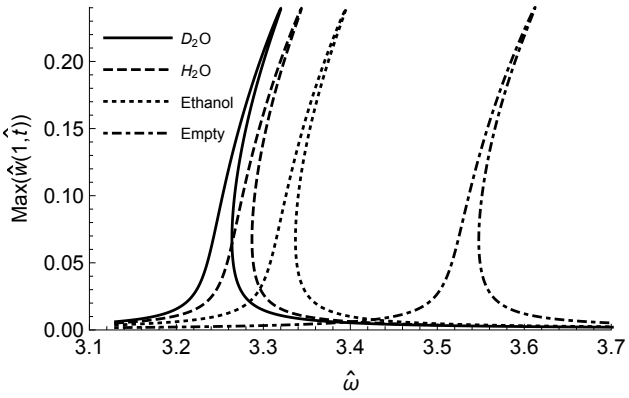


Figure 9: Influence of fluid on the non-linear frequency response curves ($\hat{Z} = 0.0003$). —— beam filled with deuterium oxide ($\rho_{D_2O} = 1100kg/m^3$), – – – water ($\rho_{H_2O} = 1000kg/m^3$), –·–·– empty beam, ····· channel filled with Ethanol ($\rho_{EtOH} = 790kg/m^3$).

Figure $10(a)$ shows the maximum deflection of the hollow cantilever under the action of the moving particle (passing only the first leg) when $\hat{Z} = 0.00011$ and $\hat{\omega} = 3.278$. As it can be seen from the figure, for this set of excitation values, the time response is characterized by a jump between points $D$ and $E$. This non-linear behavior is better explained in Figure $10(b)$.

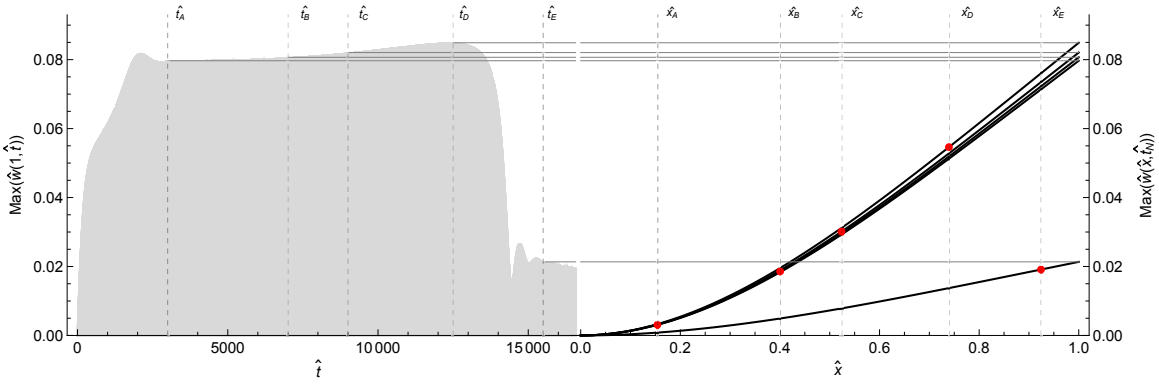


(a)

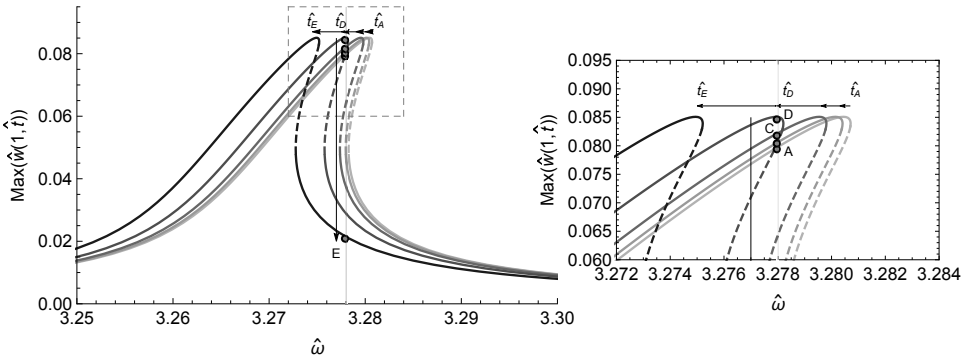


(b)

Figure 10: Maximum deflection of the beam under the action of the moving particle when the excitation frequency and amplitude are fixed at $\hat{\omega} = 3.278$ and $\hat{Z} = 0.00011$, and particle velocity is $0.004m/s$. Points $A$-$E$ depict different time instants at which the particle lies at specific position along the channel. (a) Time response along one leg of the beam with the corresponding maximum deflection. (b). Frequency response curve translation due to the particle movement. The upper horizontal arrows indicate the translation of the resonant peak and dashed lines indicate unstable solutions.

Once the cantilever is excited at a frequency close to the resonant frequency, with the motion

of the particle, the natural frequency decreases in time, until a saddle-node bifurcation is reached. At this point, the response jumps from a large limit cycle to a small one and as a matter of fact the amplitude of the response greatly decreases (point $E$). It is worth noting that, after the jump, the cantilever exhibits a new transient behaviour at the onset of the motion of the lower amplitude branch. Observation of the non-linear behavior, similar to the linear case, highly depends on the excitation frequency. This can also be seen from the time response envelopes of the beam-particle interaction at frequency offsets relative to the resonant frequency in Figure 11.

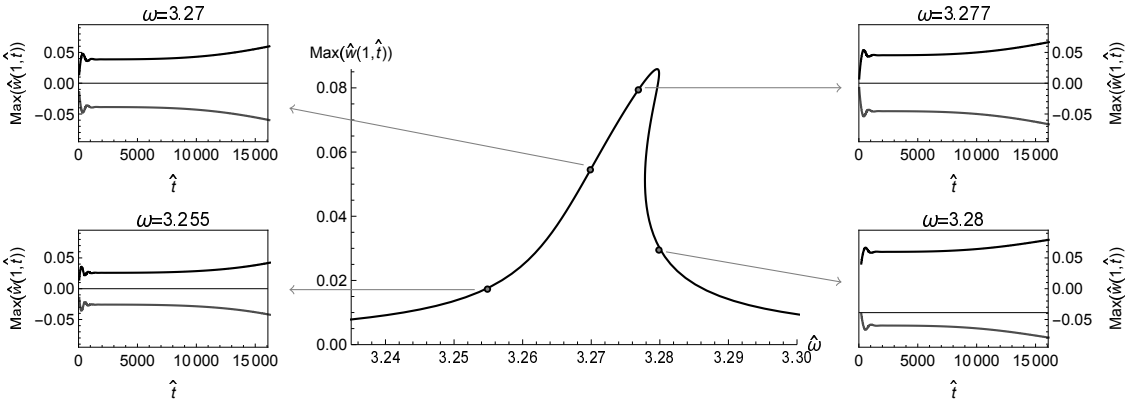


Figure 11: Time response envelops of the hollow cantilever excited at different excitation frequencies and subjected to moving particle towards the primary leg only. The parameters are the same as those indicated in Figure 10.

Figure 12 shows the transition from linear to non-linear response and the time history of the cantilever as the particle passes the first leg. It can be seen that comparing to linear case, in non-linear regime the amplitude drop due to particle movement could be detected with a much higher resolution.

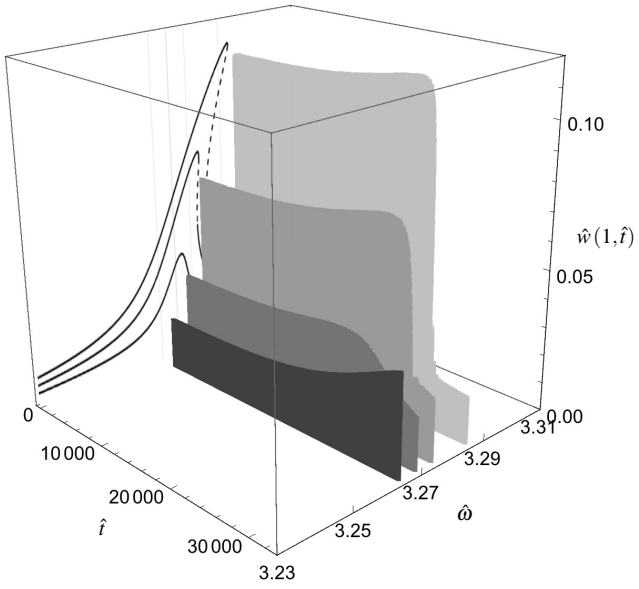


Figure 12: Transition between linear and non-linear response with different time history shapes. Sets of parameters: $(\hat{Z},\hat{\omega}) = \{(0.00005,3.265),(0.00005,3.27),(0.0001,3.275),(0.00015,3.285)\}$. Particle velocity $0.002m/s$.

The frequency variation in time for both linear and non-linear cases while particle is passing both legs is shown in Figure 13 . The jump down behavior found in the time response is associated

with a sudden frequency-drop (solid line), indicating better frequency resolution with respect to the linear case (dashed line). It can be also observed that by operating the hollow cantilever in the non-linear regime the behaviour in the two legs becomes more asymmetric. In this case, the second frequency drop during the outgoing travel of the particle (i.e. particle passing the second leg) is different from the first frequency drop and it is due to a jump-up phenomenon from a lower to an upper stable branch.

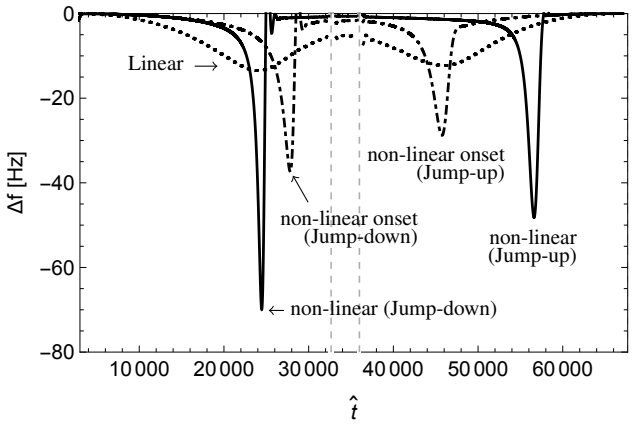


Figure 13: Frequency drop in time (full particle travel) for different excitation amplitudes and frequencies. – – – $\hat{Z} = 0.00003$ - $\hat{\omega} = 3.27$, –·–·– $\hat{Z} = 0.00008$ - $\hat{\omega} = 3.273$, —— $\hat{Z} = 0.0001$ - $\hat{\omega} = 3.277$.

## 5. Conclusions

Linear and non-linear vibrations of hollow microcantilevers interacting with small particles in liquid environment have been investigated. The microcantilever is subjected to base excitation and has an embedded microchannel through which a small particle flows. The equations of motion are obtained by using the extended Hamilton's principle and Galerkin's method is applied to obtain an accurate reduced-order model. The effect of excitation frequency and transient motion of the particle on the time history, frequency response curves and frequency drops (due to the added mass effect) have been analyzed in detail. It is observed that by operating the cantilever in the non-linear regime, higher resolutions could be achieved both in time and frequency domain. This is found to be due to transitions that occur with particle movement at saddle-node bifurcation points resulting in jumps in the frequency amplitude response that could be well-detected for sensing applications, potentially avoiding the use of complex frequency tracking devices.

## Appendix

*Appendix A*

Non-dimensional variables and parameters used in the dimensionless system (27):

$$\hat{s}=\frac{s}{L},\hat{X}=\frac{X}{L},\hat{m}\left(\hat{s}\right)=\frac{m\left(\hat{s}L\right)}{\rho A_1},\hat{I}\left(\hat{s}\right)=\frac{I\left(\hat{s}L\right)}{I_1},\hat{M}=\frac{M}{\rho A_1 L},$$
$$\hat{B}=\frac{B}{L},\hat{l}_i=\frac{l_i}{L},\hat{w}=\frac{w}{L},\hat{w}'=w',\hat{w}''=Lw'',\hat{H}_{\hat{l}_i}=H\left(\hat{s}-\frac{l_i}{L}\right)$$
$$\hat{t}=\frac{t}{\sqrt{\frac{EI_1}{\rho A_1 L^4}}},\hat{c}=c\frac{\sqrt{\frac{EI_1}{\rho A_1 L^4}}L^4}{EI_1},\hat{Z}=\frac{Z}{L},\hat{G}=\hat{\omega}^2\hat{Z},\hat{\delta}_\Delta\left(\hat{s}-\hat{X}\right)=\delta\left(L\left(\hat{s}-\hat{X}\right)\right),$$
$$\hat{\omega}=\frac{\omega}{\sqrt{\frac{EI_1}{\rho A_1 L^4}}},\hat{V}=\frac{V}{L\sqrt{\frac{EI_1}{\rho A_1 L^4}}},\hat{m}_f\left(\hat{s}\right)=\frac{m_f\left(\hat{s}L\right)}{\rho A_1} \tag{.1}$$

*Appendix B*

The constants $I_i$ for $i=1,..11$ of Eqs.(31)-(32) obtained by applying Galerkin method:

$$I_{1jn}=\int_0^1 \hat{m}\left(\hat{s}\right)\phi_n\left(\hat{s}\right)\phi_j\left(\hat{x}\right)d\hat{s} \tag{.2}$$

$$I_{2jn}=\int_0^1 \left(\hat{I}\left(\hat{s}\right)\phi_n''\left(\hat{s}\right)\right)''\phi_j\left(\hat{s}\right)d\hat{s} \tag{.3}$$

$$I_{3jnmk}=\int_0^1 \left(\hat{I}\left(\hat{s}\right)\phi_n'\left(\hat{s}\right)\phi_m''\left(\hat{s}\right)\phi_k''\left(\hat{s}\right)\right)'\phi_j\left(\hat{s}\right)d\hat{s} \tag{.4}$$

$$I_{4jnmk}=\int_0^1 \left(\phi_n'\left(\hat{s}\right)\phi_m'\left(\hat{s}\right)\left(\hat{I}\left(\hat{s}\right)\phi_k''\left(\hat{s}\right)\right)'\right)'\phi_j\left(\hat{s}\right)d\hat{s} \tag{.5}$$

$$I_{5jnmk}=\int_0^1 \phi_j\left(\hat{s}\right)\left(\phi_n'\left(\hat{s}\right)\int_1^{\hat{s}}\hat{m}\left(\hat{s}\right)\left(\int_0^{\hat{s}}\phi_m'\left(\hat{s}\right)\phi_k'\left(\hat{s}\right)d\hat{s}\right)d\hat{s}\right)'d\hat{s} \tag{.6}$$

$$I_{6jn}=\hat{V}^2\int_0^1 \hat{m}_f\left(\hat{s}\right)\left(\hat{H}_0-\hat{H}_{\hat{l}_1}\right)\phi_n''\left(\hat{s}\right)\phi_j\left(\hat{s}\right)d\hat{s} \tag{.7}$$

$$I_{7jn}=\int_0^1 \phi_n\left(\hat{s}\right)\phi_j\left(\hat{s}\right)d\hat{s} \tag{.8}$$

$$I_{8j}=\int_0^1 \left(\hat{m}\left(\hat{s}\right)+\hat{M}\hat{\delta}_\Delta\left(\hat{s}-\hat{X}\right)\right)\phi_j\left(\hat{s}\right)d\hat{s} \tag{.9}$$

$$I_{9jnmk}=\hat{V}^2\int_0^1 \phi_j\left(\hat{s}\right)\left(\phi_n'\left(\hat{s}\right)\int_1^{\hat{s}}\hat{M}\phi_m'\left(\hat{s}\right)\phi_k'\left(\hat{s}\right)\hat{\delta}_\Delta\left(\hat{s}-\hat{X}\right)d\hat{s}\right)'d\hat{s} \tag{.10}$$

$$I_{10jnmk}=\hat{V}\int_0^1 \phi_j\left(\hat{s}\right)\left(\phi_n'\left(\hat{s}\right)\int_1^{\hat{s}}\hat{M}\phi_m'\left(\hat{s}\right)\phi_k'\left(\hat{s}\right)\hat{\delta}_\Delta\left(\hat{s}-\hat{X}\right)d\hat{s}\right)'d\hat{s} \tag{.11}$$

$$I_{11jnmk}=\int_0^1 \phi_j\left(\hat{s}\right)\left(\phi_n'\left(\hat{s}\right)\int_1^{\hat{s}}\hat{M}\left(\int_0^{\hat{s}}\phi_m'\left(\hat{s}\right)\phi_k''\left(\hat{s}\right)d\hat{s}\right)\hat{\delta}_\Delta\left(\hat{s}-\hat{X}\right)d\hat{s}\right)'d\hat{s} \tag{.12}$$

## References


[1] K.L. Ekinci. Electromechanical transducers at the nanoscale: Actuation and sensing of motion in nanoelectromechanical systems (nems). *Small*, 1(8-9):786–797, 2005.

[2] H.G. Craighead. Nanoelectromechanical systems. *Science*, 290(5496):1532–1535, 2000.

[3] M. D. LaHaye, O. Buu, B. Camarota, and K. C. Schwab. Approaching the quantum limit of a nanomechanical resonator. *Science*, 304(5667):74–77, 2004.

[4] T. P. Burg and S. R. Manalis. Suspended microchannel resonators for biomolecular detection. *Applied Physics Letters*, 83(13):2698–2700, 2003.

[5] Kyo Seon Hwang, Kilho Eom, Jeong Hoon Lee, Dong Won Chun, Byung Hak Cha, Dae Sung Yoon, Tae Song Kim, and Jung Ho Park. Dominant surface stress driven by biomolecular interactions in the dynamical response of nanomechanical microcantilevers. *Applied Physics Letters*, 89(17), 2006.

[6] John A. Judge, Douglas M. Photiadis, Joseph F. Vignola, Brian H. Houston, and Jacek Jarzynski. Attachment loss of micromechanical and nanomechanical resonators in the limits of thick and thin support structures. *Journal of Applied Physics*, 101(1), 2007.

[7] Behrouz Arash, Jin-Wu Jiang, and Timon Rabczuk. A review on nanomechanical resonators and their applications in sensors and molecular transportation. *Applied Physics Reviews*, 2(2), 2015.

[8] X. L. Feng, Rongrui He, Peidong Yang, and M. L. Roukes. Very high frequency silicon nanowire electromechanical resonators. *Nano Letters*, 7(7):1953–1959, 2007.

[9] Alexei Gaidarzhy, Guiti Zolfagharkhani, Robert L. Badzey, and Pritiraj Mohanty. Spectral response of a gigahertz-range nanomechanical oscillator. *Applied Physics Letters*, 86(25), 2005.

[10] Y. T. Yang, C. Callegari, X. L. Feng, K. L. Ekinci, and M. L. Roukes. Zeptogram-scale nanomechanical mass sensing. *Nano Letters*, 6(4):583–586, 2006. PMID: 16608248.

[11] Jungchul Lee, Wenjiang Shen, Kris Payer, Thomas P. Burg, and Scott R. Manalis. Toward attogram mass measurements in solution with suspended nanochannel resonators. *Nano Letters*, 10(7):2537–2542, 2010. PMID: 20527897.

[12] K. L. Ekinci, Y. T. Yang, and M. L. Roukes. Ultimate limits to inertial mass sensing based upon nanoelectromechanical systems. *Journal of Applied Physics*, 95(5):2682–2689, 2004.

[13] A. K. Naik, M. S. Hanay, W. K. Hiebert, X. L. Feng, and M. L. Roukes. Towards single-molecule nanomechanical mass spectrometry. *Nat Nano*, 4(7):445–450, 07 2009.

[14] J. Chaste, A. Eichler, J. Moser, G. Ceballos, RuraliR., and A. Bachtold. A nanomechanical mass sensor with yoctogram resolution. *Nat Nano*, 7(5):301–304, 05 2012.

[15] Bruno Domon and Ruedi Aebersold. Mass spectrometry and protein analysis. *Science*, 312(5771):212–217, 2006.

[16] M. Varshney, P. S. Waggoner, C. P. Tan, K. Aubin, R. A. Montagna, and H. G. Craighead. Prion protein detection using nanomechanical resonator arrays and secondary mass labeling. *Analytical Chemistry*, 80(6):2141–2148, 2008. PMID: 18271602.

[17] P. Alex Greaney and Jeffrey C. Grossman. Nanomechanical resonance spectroscopy: A novel route to ultrasensitive label-free detection. *Nano Letters*, 8(9):2648–2652, 2008. PMID: 18707177.

[18] J. Fritz, M. K. Baller, H. P. Lang, H. Rothuizen, P. Vettiger, E. Meyer, H. J. Güntherodt, Ch. Gerber, and J. K. Gimzewski. Translating biomolecular recognition into nanomechanics. *Science*, 288(5464):316–318, 2000.

[19] B. Ilic, D. Czaplewski, M. Zalalutdinov, H. G. Craighead, P. Neuzil, C. Campagnolo, and C. Batt. Single cell detection with micromechanical oscillators. *Journal of Vacuum Science and Technology B*, 19(6):2825–2828, 2001.

[20] V.-N. Nguyen, S. Baguet, C.-H. Lamarque, and R. Dufour. Bifurcation-based micro-/nanoelectromechanical mass detection. *Nonlinear Dynamics*, 79(1):647–662, 2015.

[21] V. Kumar, Y. Yang, J. W. Boley, G. T. C. Chiu, and J. F. Rhoads. Modeling, analysis, and experimental validation of a bifurcation-based microsensor. *Journal of Microelectromechanical Systems*, 21(3):549–558, June 2012.

[22] Vijay Kumar, J. William Boley, Yushi Yang, Hendrik Ekowaluyo, Jacob K. Miller, George T.-C. Chiu, and Jeffrey F. Rhoads. Bifurcation-based mass sensing using piezoelectrically-actuated microcantilevers. *Applied Physics Letters*, 98(15), 2011.

[23] Thomas Braun, Viola Barwich, Murali Krishna Ghatkesar, Adriaan H. Bredekamp, Christoph Gerber, Martin Hegner, and Hans Peter Lang. Micromechanical mass sensors for biomolecular detection in a physiological environment. *Phys. Rev. E*, 72:031907, Sep 2005.

[24] Stefan Weigert, Markus Dreier, and Martin Hegner. Frequency shifts of cantilevers vibrating in various media. *Applied Physics Letters*, 69(19):2834–2836, 1996.

[25] Thomas P. Burg, Michel Godin, Scott M. Knudsen, Wenjiang Shen, Greg Carlson, John S. Foster, Ken Babcock, and Scott R. Manalis. Weighing of biomolecules, single cells and single nanoparticles in fluid. *Nature*, 446(7139):1066–1069, 04 2007.

[26] Selim Olcum, Nathan Cermak, Steven C. Wasserman, Kathleen S. Christine, Hiroshi Atsumi, Kris R. Payer, Wenjiang Shen, Jungchul Lee, Angela M. Belcher, Sangeeta N. Bhatia, and Scott R. Manalis. Weighing nanoparticles in solution at the attogram scale. *Proceedings of the National Academy of Sciences*, 111(4):1310–1315, 2014.

[27] J.E. Sader, T.P. Burg, and S.R. Manalis. Energy dissipation in microfluidic beam resonators. *Journal of Fluid Mechanics*, 650:215–250, 5 2010.

[28] Wen-Ming Zhang, Han Yan, Hui-Ming Jiang, Kai-Ming Hu, Zhi-Ke Peng, and Guang Meng. Dynamics of suspended microchannel resonators conveying opposite internal fluid flow: Stability, frequency shift and energy dissipation. *Journal of Sound and Vibration*, 368:103 – 120, 2016.

[29] Thomas P. Burg, John E. Sader, and Scott R. Manalis. Nonmonotonic energy dissipation in microfluidic resonators. *Phys. Rev. Lett.*, 102:228103, Jun 2009.

[30] John E. Sader, Thomas P. Burg, Jungchul Lee, and Scott R. Manalis. Energy dissipation in microfluidic beam resonators: Effect of poisson's ratio. *Phys. Rev. E*, 84:026304, Aug 2011.

[31] John E. Sader, Jungchul Lee, and Scott R. Manalis. Energy dissipation in microfluidic beam resonators: Dependence on mode number. *Journal of Applied Physics*, 108(11), 2010.

[32] T. S. Hug, T. Biss, N. F. de Rooij, and U. Staufer. Generic fabrication technology for transparent and suspended microfluidic and nanofluidic channels. In *The 13th International Conference on Solid-State Sensors, Actuators and Microsystems, 2005. Digest of Technical Papers. TRANSDUCERS '05.*, volume 2, pages 1191–1194 Vol. 2, 2005.

[33] A. Erturk and D.J. Inman. On mechanical modeling of cantilevered piezoelectric vibration energy harvesters. *Journal of Intelligent Material Systems and Structures*, 19(11):1311–1325, 2008.

[34] M.P. Paidoussis. *Fluid-Structure Interactions: Slender Structures and Axial Flow*. Fluid-structure Interactions: Slender Structures and Axial Flow, Volume 1, Second Edition. Elsevier Science, 2013.

[35] M. R. M. Crespo da Silva and C. C. Glynn. Nonlinear flexural-flexural-torsional dynamics of inextensional beams. i. equations of motion. *Journal of Structural Mechanics*, 6(4):437–448, 1978.

[36] Sultan A. Q. Siddiqui, M. Farid Golnaraghi, and Glenn R. Heppler. Dynamics of a flexible cantilever beam carrying a moving mass. *Nonlinear Dynamics*, 15(2):137–154, 1998.

[37] S. Hornstein and O. Gottlieb. Nonlinear dynamics, stability and control of the scan process in noncontacting atomic force microscopy. *Nonlinear Dynamics*, 54(1):93–122, 2008.

[38] Eusebius J. Doedel, Alan R. Champneys, Thomas F. Fairgrieve, Yuri A. Kuznetsov, Bjorn Sandstede, and Xianjun Wang. Auto 97: Continuation and bifurcation software for ordinary differential equations (with homcont).

[39] Murali Krishna Ghatkesar, Hector Hugo Perez Garza, and Urs Staufer. Hollow afm cantilever pipette. *Microelectronic Engineering*, 124:22 – 25, 2014. Micro/Nano Biotechnologies and Systems 2013.

[40] J. Sader and J. Friend. Note: Calibration of atomic force microscope cantilevers using only their resonant frequency and quality factor. *Review of Scientific Instruments*, 85(11), 2014.

[41] S.Nima Mahmoodi, Mohammed F. Daqaq, and Nader Jalili. On the nonlinear-flexural response of piezoelectrically driven microcantilever sensors. *Sensors and Actuators A: Physical*, 153(2):171 – 179, 2009.